Sequence Impedance Modeling and Stability Analysis for Load Converters With Inertial Support

Yifeng Liu, Xiaoping Zhou, *Student Member, IEEE*, Yandong Chen, *Senior Member, IEEE*, Leming Zhou, *Member, IEEE*, Lei Wang, *Member, IEEE*, and Wenhua Wu, *Student Member, IEEE*

***Abstract*—Load converters with inertial support are used to enhance the system inertia. However, these converters may fail to operate stably in the weak grid. In this article, sequence impedance modeling and stability comparison analysis are proposed for the load virtual synchronous machine (LVSM) and the load converter with virtual inertia control (LCVIC). First, the universal sequence impedance formulas are derived by considering dc-link voltage dynamics and frequency-coupling effects. Then, the precise sequence impedance models are built for impedance characteristics analysis of LVSM and LCVIC. The analysis shows that the positive-sequence impedance of LVSM is generally inductive in the middle-frequency band, which is basically consistent with the grid impedance. In contrast, the positive-sequence impedance of LCVIC is negative-resistive-capacitive (i.e., phase angle is between $-180°$ and $-90°$) in the middle-frequency band, which may lead to harmonic oscillation in the weak grid. Furthermore, the effects of grid impedance, load power, and other control parameters on the stability are analyzed for the two load converters based on the derived model and Nyquist stability criterion. The analysis results reveal that LVSM has better stability than LCVIC in the weak grid. Finally, the experimental results validate the correctness of the theoretical analyses.**

***Index Terms*—Harmonic oscillation, load converter, sequence impedance modeling, stability analysis, virtual inertia, weak grid.**

I. Introduction

RENEWABLE energy sources and load converters are increasingly connected to modern power systems, such as photovoltaic power generation, wind power generation, motor drive systems, high-voltage direct current (HVdc) transmission systems, etc. [1]–[4], leading to the weakened system inertia. To address this issue, the virtual synchronous machine (VSM) technology is proposed in [5], which mimics the inertia and droop mechanisms of the synchronous generator. Moreover, the VSM technology is suggested by several other authors to control load converters [6]–[11]. In [6], a novel load VSM (LVSM) control strategy is proposed to get rid of the synchronization unit for pulsewidth modulation controlled rectifiers. In [7], the LVSM is proposed to achieve the goal of stabilizing dc-link voltage under the unbalanced voltage condition. As for HVdc systems, the LVSM is proposed for the sending-end rectifier in [8] and [9], which enables it to provide inertial support for the utility grid during the dynamic process. Moreover, the load converter with virtual inertia control (LCVIC) is proposed in [10] and [11], which is realized by proportionally linking the dc-link capacitor voltage with the grid frequency.

Another significant problem is that the load converters may fail to operate stably in the weak grid [9], [11]–[15]. To reveal this issue, the closed-loop transfer function model of the rectifier station is built for the parameter design and the stability analysis of the LVSM in [9], which indicates that the virtual moment of inertia and the proportional integral (PI) gains can directly impact on the phase margin of the system. In [11], the stability analysis is proposed for the LCVIC based on the closed-loop dc-link voltage transfer function, which reveals that the virtual inertia control may induce instability to the power converters under weak grid conditions. Moreover, the impedance models of the load converter are developed in the synchronous reference (d–q) frame in [12] and [13], which indicates the instability issues induced by the constant power load behavior and phase-locked loop (PLL) dynamics. Nevertheless, these derived models overlook the impact of the dc-link voltage control on cross-couplings between d- and q-axis dynamics. Thus, the d–q domain impedance model including the dc-link voltage dynamics is developed for the load converter in [14], which indicates that the dc-link voltage control can lead to low-frequency oscillations in the rectifier mode and high-frequency oscillations in the inverter mode. Furthermore, Li *et al.* in [15] derive the d–q domain impedance model for the static synchronous compensator (STATCOM) involving the dynamics of PLL, output current, ac voltage, and dc voltage loops, which demonstrates that STATCOM may suffer instability due to the parameters changes in these control loops.

Yet, all the aforementioned literature mainly analyzes the stability of the load converters by means of the close-loop transfer function or the d–q domain impedance model, which cannot give a clear physical interpretation for the system interaction stability [16]. In regard to this issue, Cespedes and Sun in [17] propose the sequence impedance modeling method for the grid-connected converter in the three-phase stationary reference frame by applying the harmonic linearization method, which is also widely

Manuscript received September 25, 2019; revised January 30, 2020 and April 8, 2020; accepted May 14, 2020. Date of publication May 18, 2020; date of current version July 31, 2020. This work was supported in part by the National Natural Science Foundation of China under Grant 51907058, in part by the Postdoctoral Innovative Talent Support Program of China under Grant BX20180095, and in part by the China Postdoctoral Science Foundation under Grant 2018M640747. Recommended for publication by Associate Editor C. Fernandez. (*Corresponding author: Xiaoping Zhou.*)

The authors are with the College of Electrical and Information Engineering, Hunan University, Changsha 410082, China (e-mail: 573430757@qq.com; zxp2011@hnu.edu.cn; yandong_chen@hnu.ed.cn; leming_zhou@126.com; jordanwanglei@gmail.com; wenhua_5@163.com).

Color versions of one or more of the figures in this article are available online at https://ieeexplore.ieee.org.

Digital Object Identifier 10.1109/TPEL.2020.2995804

adopted in HVdc transmission, grid-tied wind system, modular multilevel converter, and virtual synchronous generator [18]–[22]. In [21] and [22], the sequence impedance models are built for the VSM. The stabilities of the voltage-controlled VSM, current-controlled VSM, and traditional grid-connected inverters are compared and analyzed, which give a clear physical interpretation for the system interaction stability. Nevertheless, in [21] and [22], the derived sequence impedance models of the inverters overlook the frequency-coupling effects brought by the *d*–*q* transformation. Besides, the dc-link voltage control can cause harmonic interactions between the ac side and the dc side of the converter, which also affects the frequency-coupling components [23]–[26]. Furthermore, the abovementioned sequence impedance modeling and stability studies for the grid-connected converters mainly focus on the source-side converter. To the author's best knowledge, there is no literature to analyze and compare the stability of load converters with inertial support based on the sequence impedance model.

Therefore, considering the abovementioned issues, this article derives the precise sequence impedance models for the LCVIC and the LVSM, and compares their operational stability in the weak grid. The rest of this article is organized as follows. Section II derives the precise sequence impedance models of the LCVIC and the LVSM considering dc-link voltage dynamics and frequency-coupling effects. Section III verifies the sequence impedance models of the two load converters, and compares their impedance characteristics. Section IV discusses the impedance ratio for the stability analysis of the LCVIC and the LVSM. Thereupon, the Nyquist stability criterion (NSC) is used to analyze the effects of grid impedance, load power, and other control parameters on the stability of the two load converters. Then, the effectiveness of the derived sequence impedance model and stability analysis is confirmed by experiment in Section V. Finally, the conclusion is drawn in Section VI.

II. Sequence Impedance Modeling of the LCVIC and the LVSM

A. Universal Sequence Impedance Calculation Formulas for Two Load Converters

To facilitate the sequence impedance modeling of the two load converters (i.e., the LCVIC and the LVSM), this section derives the universal sequence impedance calculation formulas by means of the harmonic linearization method [16]. The universal calculation formulas are developed from the power stage small-signal model of the load converter, which involves the frequency-coupling effects and the dc-link voltage dynamics.

The topology of the load converter is given in Fig. 1, which is connected to the grid at the point of common coupling through the *LC* filter. In Fig. 1, v_x, i_x, and m_x are the three-phase input voltages, currents, and modulating signals, respectively, where *x* stands for phase *a*, *b* and *c*; $v_{\rm dc}$ and $i_{\rm dc}$ are the dc-link output voltage and current, respectively; L_g and R_g are the equivalent line inductance and resistance, respectively; L_f, C_f, and R_d are the filter inductance, filter capacitance, and damping resistance, respectively; and $C_{\rm dc}$ and R_L are the dc-link capacitor and dc-link load, respectively.

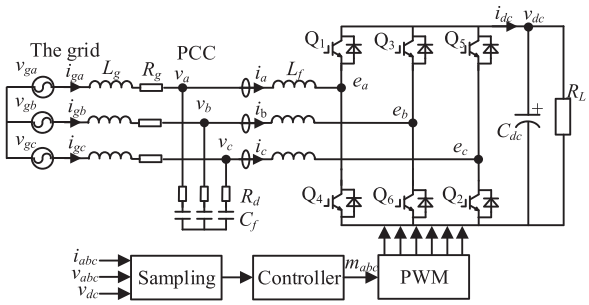

Fig. 1. Topology of the load converter.

According to Fig. 1, considering a balanced three-phase system without the neutral connection, the power stage average model can be expressed in the time domain as follows [27]:

$$L_f \frac{d}{dt}\begin{bmatrix} i_a \\ i_b \\ i_c \end{bmatrix} = \begin{bmatrix} v_a \\ v_b \\ v_c \end{bmatrix} - K_m \begin{bmatrix} m_a \\ m_b \\ m_c \end{bmatrix} v_{\rm dc} \tag{1}$$

$$i_{\rm dc} = K_m(m_a i_a + m_b i_b + m_c i_c) \tag{2}$$

$$i_{\rm dc} = C_{\rm dc}\frac{dv_{\rm dc}}{dt} + \frac{v_{\rm dc}}{R_L} \tag{3}$$

where K_m is the modulator gain.

In order to derive the sequence impedance of the load converter, a positive-sequence voltage perturbation at frequency f_p is usually injected into the ac input terminal of the load converter [17]. The influence of grid impedance is ignored at first. Then, the phase-A input voltage of the load converter can be expressed in the time and frequency domain as follows:

$$v_a(t) = V_1\cos(2\pi f_1 t) + V_p\cos(2\pi f_p t + \varphi_{vp}) \tag{4}$$

$$\mathbf{V}_a[f] = \begin{cases} \mathbf{V}_{\pm 1}, & f = \pm f_1 \\ \mathbf{V}_{\pm p}, & f = \pm f_p \end{cases} \tag{5}$$

where subscripts + and – represent positive- and negative-frequency components in the frequency domain, respectively; $\mathbf{V}_{\pm 1} = V_1/2$ represents the fundamental voltage at frequency f_1; V_1 is the magnitudes of fundamental voltage; $\mathbf{V}_{\pm p} = (V_p/2)e^{\pm j\varphi_{vp}}$ represents the positive-sequence voltage perturbation at frequency f_p; and V_p and φ_{vp} are the magnitude and initial phase of the positive-sequence voltage perturbation, respectively.

According to the frequency-coupling effects of the converter [23], [28], $\mathbf{V}_p$ can produce the positive-sequence current perturbation $\mathbf{I}_p$ at frequency f_p, the coupling-negative-sequence current perturbation $\mathbf{I}_{p2}$ at frequency $f_p - 2f_1$, and the dc-link voltage perturbation $\mathbf{V}_{dp}$ at frequency $f_p - f_1$. Furthermore, the small-signal voltage and current perturbations are transferred to the modulating signal in control by sampling. Therefore, the phase-A current, the dc-link voltage, and the phase-A modulating signal in the frequency domain can be written as follows:

$$\mathbf{I}_a[f] = \begin{cases} \mathbf{I}_{\pm 1}, & f = \pm f_1 \\ \mathbf{I}_{\pm p}, & f = \pm f_p \\ \mathbf{I}_{\pm p2}, & f = \pm(f_p - 2f_1) \end{cases} \tag{6}$$

$$\mathbf{V}_{\mathrm{dc}}[f]=\begin{cases}V_{\mathrm{dc}}, & f=0\\ \mathbf{V}_{\pm dp}, & f=\pm(f_p-f_1)\end{cases},\mathbf{M}_a[f]$$
$$=\begin{cases}\mathbf{M}_{\pm 1}, & f=\pm f_1\\ \mathbf{M}_{\pm p}, & f=\pm f_p\\ \mathbf{M}_{\pm p2}, & f=\pm(f_p-2f_1)\end{cases} \tag{7}$$

where V_{dc} denotes the dc-link voltage reference; $\mathbf{I}_{\pm 1}$ denotes the fundamental current; $\mathbf{M}_{\pm 1}=(\mathbf{V}_{\pm 1}-sL_f\mathbf{I}_{\pm 1})/(K_mV_{\mathrm{dc}})$ denotes the fundamental modulating signal; $\mathbf{M}_{\pm p}$ and $\mathbf{M}_{\pm p2}$ denote the modulating signal perturbation at frequency f_p and frequency f_p-2f_1, respectively.

By substituting (5)–(7) into (1)–(3), and linearizing the frequency-domain model around its fundamental operating point, the power stage small-signal model can be expressed in the frequency domain as follows:

$$sL_f\mathbf{I}_p=\mathbf{V}_p-K_mV_{\mathrm{dc}}\mathbf{M}_p-K_m\mathbf{M}_1\mathbf{V}_{dp} \tag{8}$$
$$(s-j2\omega_1)L_f\mathbf{I}_{p2}=-K_mV_{\mathrm{dc}}\mathbf{M}_{p2}-K_m\mathbf{M}_{-1}\mathbf{V}_{dp} \tag{9}$$
$$[(s-j\omega_1)C_{\mathrm{dc}}+1/R_L]\mathbf{V}_{dp}$$
$$=3K_m(\mathbf{M}_p\mathbf{I}_{-1}+\mathbf{M}_{p2}\mathbf{I}_1+\mathbf{M}_{-1}\mathbf{I}_p+\mathbf{M}_1\mathbf{I}_{p2}) \tag{10}$$

where ω_1 denotes the fundamental angular frequency.

Generally, according to the control scheme of the converter, the relationship among m_a, i_a, v_a, and v_{dc} can be linearized in the frequency domain by using the harmonic linearization method [20]. Therefore, under the positive-sequence voltage perturbation at f_p on the ac side of the load converter, $\mathbf{M}_{\pm p}$ and $\mathbf{M}_{\pm p2}$ can be expressed as follows:

$$\begin{cases}\mathbf{M}_{\pm p}=A_{\pm p}(s)\mathbf{I}_{\pm p}+B_{\pm p}(s)\mathbf{I}_{\pm p2}\\ \qquad\quad +C_{\pm p}(s)\mathbf{V}_{\pm p}+F_{\pm p}(s)\mathbf{V}_{\pm dp}, \quad f=\pm f_p\\ \mathbf{M}_{\pm p2}=A_{\pm p2}(s)\mathbf{I}_{\pm p}+B_{\pm p2}(s)\mathbf{I}_{\pm p2}\\ \qquad\quad +C_{\pm p2}(s)\mathbf{V}_{\pm p}+F_{\pm p2}(s)\mathbf{V}_{\pm dp}, \quad f=\pm(f_p-2f_1)\end{cases} \tag{11}$$

where A(s), B(s), C(s), and F(s) denote the influence coefficients of the ac current perturbation, the coupling ac current perturbation, the ac voltage perturbation, and the dc voltage perturbation on the modulating signal perturbation, respectively. The coefficient subscripts p and $p2$ correspond to the perturbation frequencies f_p and f_p-2f_1, respectively. Consequently, by substituting (11) into (8)–(10), the universal calculation formulas for admittances $Y_{pp}(s)=\mathbf{I}_p/\mathbf{V}_p$ and $Y_{pn}(s)=\mathbf{I}_{p2}/\mathbf{V}_p$ can be calculated as (16) and (17) shown at the bottom of the next page, respectively, where $|\cdot|$ represents the determinant operator.

Moreover, considering the influence of the grid impedance $Z_g(s)$, the perturbation transfer process can be shown in Fig. 2. Then, the multi-input multioutput (MIMO) sequence admittance matrix can be obtained as

$$\begin{bmatrix}\mathbf{I}''_p\\ \mathbf{I}''_{p2}\end{bmatrix}=\begin{bmatrix}\mathbf{I}_p+\mathbf{I}'_p\\ \mathbf{I}_{p2}+\mathbf{I}'_{p2}\end{bmatrix}=\begin{bmatrix}Y_{pp}(s) & Y_{np}(s)\\ Y_{pn}(s) & Y_{nn}(s)\end{bmatrix}\begin{bmatrix}\mathbf{V}_p\\ \mathbf{V}_{p2}\end{bmatrix} \tag{12}$$

where $\mathbf{I}''_p$ and $\mathbf{I}''_{p2}$ represent the total positive-sequence current response and the total coupling-negative-sequence current response, respectively; $\mathbf{V}_{p2}$ represents the coupling-negative-sequence voltage produced by $\mathbf{I}''_{p2}$ through the grid impedance; $\mathbf{I}'_p$ and $\mathbf{I}'_{p2}$ represent the positive-sequence current response and the coupling-negative-sequence current response produced by $\mathbf{V}_{p2}$ through the load converter, respectively. Considering the conjugate relationship of the sequence impedance [29], the admittances $Y_{np}(s)$ and $Y_{nn}(s)$ can be obtained as $Y_{np}(s)=Y^*_{pn}(s-j2\omega_1)$ and $Y_{nn}(s)=Y^*_{pp}(s-j2\omega_1)$, respectively

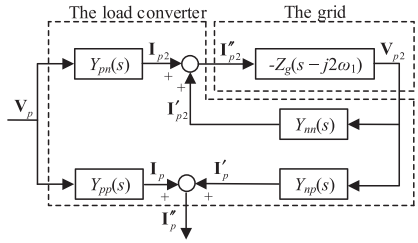

Fig. 2. Small-signal block diagram of the grid and load converter system under the positive-sequence voltage perturbation.

Therefore, according to (12), (16), and (17), the MIMO sequence admittance model can be obtained. Then, the stability analyses can be performed based on the MIMO model and the generalized Nyquist criterion [28], [29]. However, compared with the MIMO model, the single-input single-output (SISO) model is relatively convenient to analyze the interaction stability between the load converter and the grid. In fact, the work in [24]–[26] reported that the MIMO sequence impedance model can be converted to the SISO sequence impedance model with the same marginal stability condition. The SISO sequence impedance model can be defined as follows:

$$\begin{bmatrix}\mathbf{V}_p\\ \mathbf{V}_n\end{bmatrix}=\begin{bmatrix}Z_p(s) & 0\\ 0 & Z_n(s)\end{bmatrix}\begin{bmatrix}\mathbf{I}''_p\\ \mathbf{I}''_n\end{bmatrix} \tag{13}$$

where $\mathbf{V}_n$ and $\mathbf{I}''_n$ represent the negative-sequence voltage perturbation at f_n and the total negative-sequence current response at f_n, respectively, which are measured at the ac input terminal of the load converter after another negative-sequence perturbation injection at f_n.

Then, according to Fig. 2 and (12), the positive-sequence impedance $Z_p(s)$ of the load converter can be calculated as follows:

$$Z_p(s)=\frac{\mathbf{V}_p}{\mathbf{I}''_p}=\left[Y_{pp}(s)-\frac{Y_{pn}(s)Y_{np}(s)Z_g(s-j2\omega_1)}{1+Z_g(s-j2\omega_1)Y_{nn}(s)}\right]^{-1}$$
$$=\left[Y_{pp}(s)-\frac{Y_{pn}(s)Y^*_{pn}(s-j2\omega_1)}{Y_g(s-j2\omega_1)+Y^*_{pp}(s-j2\omega_1)}\right]^{-1}. \tag{14}$$

Moreover, to derive negative-sequence impedance $Z_n(s)$ of the load converter, the negative-sequence voltage perturbation at frequency f_n is injected into the ac side of the load converter. And the derivation process is the same as $Z_p(s)$. In fact, considering the conjugate relationship of the sequence impedance [29], $Z_n(s)$ can be handily calculated as follows:

$$Z_n(s)=\frac{\mathbf{V}_n}{\mathbf{I}''_n}=Z^*_p(s)$$
$$=\left[Y^*_{pp}(s)-\frac{Y^*_{pn}(s)Y_{pn}(s+j2\omega_1)}{Y_g(s+j2\omega_1)+Y_{pp}(s+j2\omega_1)}\right]^{-1}. \tag{15}$$

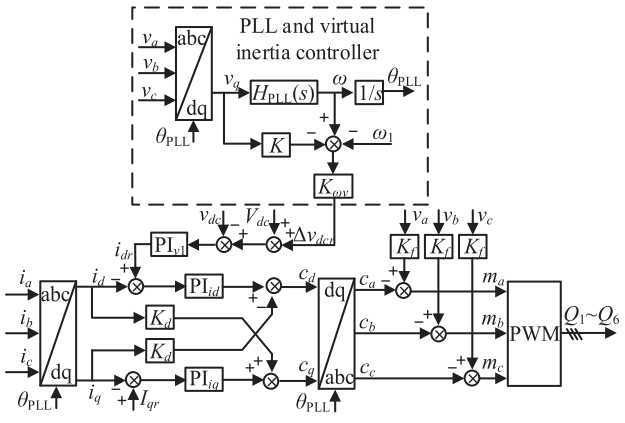

Fig. 3. Control diagram of the LCVIC.

Therefore, according to (14)–(17), the universal calculation formulas for the SISO sequence impedance model of the LCVIC and the LVSM are obtained, which can be used to analyze the small-signal stability by applying the NSC [21], [24].

B. Sequence Impedance Modeling of the LCVIC

Fig. 3 shows the control diagram of the LCVIC [11]. The virtual inertia can be obtained from the dc-link capacitor by utilizing the characteristics of capacitor absorption/release energy. The dc-link capacitor voltage and the grid frequency are linked by the inertia control gain $K_{\omega v}$, so the fluctuation of the grid frequency can be suppressed by regulating the active power of the converter.

The PLL output angle can be expressed as $\theta_{\rm PLL} = \theta_1 + \Delta\theta$, where θ_1 is the phase angle of the fundamental voltage and $\Delta\theta$ is the small-signal perturbation of the PLL output angle. According to [17], the transfer function from the positive-sequence voltage perturbation $\mathbf{V}_p$ at frequency f_p to the PLL output phase perturbation $\Delta\theta_{p1}$ at frequency $f_p - f_1$ can be expressed as follows:

$$G_p(s) = \Delta\theta_{\pm p1}/\mathbf{V}_{\pm p} = \mp jT_{\rm PLL}(s)G_v(s \pm j\omega_1) \tag{18}$$

$$T_{\rm PLL}(s) = H_{\rm PLL}(s)/[s + V_1 H_{\rm PLL}(s)] \tag{19}$$

where $G_v(s) = 1/(1 + sT_v)$ represents the transfer function of the voltage sampling filter; $H_{\rm PLL}(s) = k_{pp} + k_{pi}/s$ represents the transfer function of the PLL controller; T_v is the time constant of the input voltage sampling filter; k_{pp} and k_{pi} are proportional and integral gains of the PLL controller, respectively.

Moreover, Park's transformation is defined as follows:

$$T(\theta_{\rm PLL}) = \frac{2}{3}\begin{bmatrix} \cos\theta_{\rm PLL} & \cos(\theta_{\rm PLL} - 2\pi/3) & \cos(\theta_{\rm PLL} + 2\pi/3) \\ -\sin\theta_{\rm PLL} & -\sin(\theta_{\rm PLL} - 2\pi/3) & -\sin(\theta_{\rm PLL} + 2\pi/3) \\ 1/2 & 1/2 & 1/2 \end{bmatrix}. \tag{20}$$

Then, the calculation of currents i_d and i_q in the *d–q* frame can be expressed as follows:

$$[\,i_d \quad i_q \quad 0\,]^T = T(\theta_{\rm PLL}) \cdot [\,i_a \quad i_b \quad i_c\,]^T. \tag{21}$$

Note that $\cos\ \theta_{\rm PLL} \approx \cos\theta_1 - \Delta\theta \sin\theta_1$ and $\sin\theta_{\rm PLL} \approx \sin\theta_1 + \Delta\theta\cos\theta_1$. Then, by substituting (18)–(20) and (6) into (21), and applying the frequency-domain convolution theorem [28], the frequency-domain expressions of i_d and i_q can be

$$Y_{pp}(s) = \frac{\mathbf{I}_p}{\mathbf{V}_p} = \frac{\begin{vmatrix} 1 - K_m V_{\rm dc} C_p(s) & K_m V_{\rm dc} B_p(s) & K_m V_{\rm dc} F_p(s) + K_m \mathbf{M}_1 \\ -K_m V_{\rm dc} C_{p2}(s - j2\omega_1) & (s - j2\omega_1)L_f + K_m V_{\rm dc} B_{p2}(s - j2\omega_1) & K_m V_{\rm dc} F_{p2}(s - j2\omega_1) + K_m \mathbf{M}_{-1} \\ -\mathbf{I}_{-1} C_p(s) - \mathbf{I}_1 C_{p2}(s - j2\omega_1) & \mathbf{I}_{-1} B_p(s) + \mathbf{I}_1 B_{p2}(s - j2\omega_1) + \mathbf{M}_1 & -[(s - j\omega_1)C_{\rm dc} + 1/R_L]/(3K_m) \\ & & + \mathbf{I}_{-1} F_p(s) + \mathbf{I}_1 F_{p2}(s - j2\omega_1) \end{vmatrix}}{\begin{vmatrix} sL_f + K_m V_{\rm dc} A_p(s) & K_m V_{\rm dc} B_p(s) & K_m V_{\rm dc} F_p(s) + K_m \mathbf{M}_1 \\ K_m V_{\rm dc} A_{p2}(s - j2\omega_1) & (s - j2\omega_1)L_f + K_m V_{\rm dc} B_{p2}(s - j2\omega_1) & K_m V_{\rm dc} F_{p2}(s - j2\omega_1) + K_m \mathbf{M}_{-1} \\ \mathbf{I}_{-1} A_p(s) + \mathbf{I}_1 A_{p2}(s - j2\omega_1) + \mathbf{M}_{-1} & \mathbf{I}_{-1} B_p(s) + \mathbf{I}_1 B_{p2}(s - j2\omega_1) + \mathbf{M}_1 & -[(s - j\omega_1)C_{\rm dc} + 1/R_L]/(3K_m) \\ & & + \mathbf{I}_{-1} F_p(s) + \mathbf{I}_1 F_{p2}(s - j2\omega_1) \end{vmatrix}} \tag{16}$$

$$Y_{pn}(s) = \frac{\mathbf{I}_{p2}}{\mathbf{V}_p} = \frac{\begin{vmatrix} sL_f + K_m V_{\rm dc} A_p(s) & 1 - K_m V_{\rm dc} C_p(s) & K_m V_{\rm dc} F_p(s) + K_m \mathbf{M}_1 \\ K_m V_{\rm dc} A_{p2}(s - j2\omega_1) & -K_m V_{\rm dc} C_{p2}(s - j2\omega_1) & K_m V_{\rm dc} F_{p2}(s - j2\omega_1) + K_m \mathbf{M}_{-1} \\ \mathbf{I}_{-1} A_p(s) + \mathbf{I}_1 A_{p2}(s - j2\omega_1) + \mathbf{M}_{-1} & -\mathbf{I}_{-1} C_p(s) - \mathbf{I}_1 C_{p2}(s - j2\omega_1) & -[(s - j\omega_1)C_{\rm dc} + 1/R_L]/(3K_m) \\ & & + \mathbf{I}_{-1} F_p(s) + \mathbf{I}_1 F_{p2}(s - j2\omega_1) \end{vmatrix}}{\begin{vmatrix} sL_f + K_m V_{\rm dc} A_p(s) & K_m V_{\rm dc} B_p(s) & K_m V_{\rm dc} F_p(s) + K_m \mathbf{M}_1 \\ K_m V_{\rm dc} A_{p2}(s - j2\omega_1) & (s - j2\omega_1)L_f + K_m V_{\rm dc} B_{p2}(s - j2\omega_1) & K_m V_{\rm dc} F_{p2}(s - j2\omega_1) + K_m \mathbf{M}_{-1} \\ \mathbf{I}_{-1} A_p(s) + \mathbf{I}_1 A_{p2}(s - j2\omega_1) + \mathbf{M}_{-1} & \mathbf{I}_{-1} B_p(s) + \mathbf{I}_1 B_{p2}(s - j2\omega_1) + \mathbf{M}_1 & -[(s - j\omega_1)C_{\rm dc} + 1/R_L]/(3K_m) \\ & & + \mathbf{I}_{-1} F_p(s) + \mathbf{I}_1 F_{p2}(s - j2\omega_1) \end{vmatrix}} \tag{17}$$

obtained as follows:

$$\mathbf{I}_d[f]=\begin{cases} I_{dr}, & f=0 \\ G_i(s\pm j\omega_1)\mathbf{I}_{\pm p} & \\ +\,G_i(s\mp j\omega_1)\mathbf{I}_{\pm p2}+I_{qr}\Delta\theta_{\pm p1}, & f=\pm(f_p-f_1) \end{cases} \tag{22}$$

$$\mathbf{I}_q[f]=\begin{cases} I_{qr}, & f=0 \\ \mp jG_i(s\pm j\omega_1)\mathbf{I}_{\pm p} & \\ \pm jG_i(s\mp j\omega_1)\mathbf{I}_{\pm p2}-I_{dr}\Delta\theta_{\pm p1}, & f=\pm\,(f_p-f_1) \end{cases} \tag{23}$$

where $G_i(s)=1/(1+sT_i)$ represents the transfer function of the current sampling filter; and T_i is the time constant of the input current sampling filter; I_{dr} and I_{qr} are the *d*- and *q*-axis current references, respectively.

According to Fig. 3, the dc-link voltage command error $\Delta v_{\rm dcr}$ induced by the virtual inertia control can be obtained as

$$\Delta v_{\rm dcr}=\frac{H_{\rm PLL}(s)-K}{H_{\rm PLL}(s)}K_{\omega v}s\Delta\theta=H_m(s)\Delta\theta \tag{24}$$

where *K* denotes a proportional gain.

Moreover, according to the dc-link voltage control and the *d*- and *q*-axis current decoupling control in Fig. 3, the modulating signals c_d and c_q in the *d*–*q* frame can be obtained as

$$c_d=[(V_{\rm dc}+\Delta v_{\rm dcr}-G_d(s)v_{\rm dc})H_{v1}(s)-i_d]H_i(s)-K_di_q \tag{25}$$

$$c_q=(I_{qr}-i_q)H_i(s)+K_di_d \tag{26}$$

where $H_{v1}(s)=k_{vp1}+k_{vi1}/s$ and $H_i(s)=k_{ip}+k_{ii}/s$ are the transfer functions of the dc-link voltage and *dq*-axis current PI controller, respectively; $G_d(s)=1/(1+sT_d)$ is the transfer function of the dc-link voltage sampling filter; k_{vp1} and k_{vi1} are proportional and integral gains of the dc-link voltage controller of the LCVIC, respectively; k_{ip} and k_{ii} are proportional and integral gains of the current controller, respectively; T_d is the time constant of the dc-link voltage sampling filter; and K_d is the decoupling gain.

Therefore, considering inverse Park's transformation and feedforward control, the modulating signal m_a can be expressed as

$$m_a=K_fG_v(s)v_a-(\cos\theta_{\rm PLL}c_d-\sin\theta_{\rm PLL}c_q) \tag{29}$$

where K_f represents the feedforward gain.

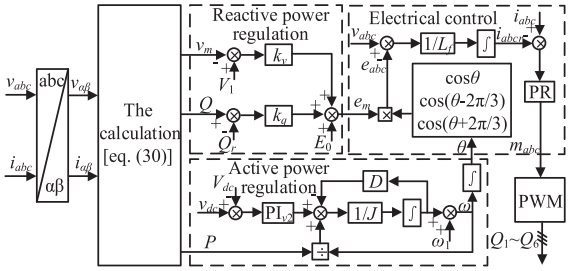

Fig. 4. Control diagram of the LVSM.

By substituting (5)–(7), and (22)–(26) into (29), and applying the frequency-domain convolution theorem, the coefficients *A*(*s*), *B*(*s*), *C*(*s*), and *F*(*s*) at frequency f_p and f_p-2f_1 in (11) can be calculated as (27) and (28), as shown at the bottom of this page, respectively. Then, by substituting (27) and (28) into the universal calculation formulas (14)–(17), the precise positive- and negative-sequence impedances $Z_{cp}(s)$ and $Z_{cn}(s)$ of the LCVIC can be calculated.

C. Sequence Impedance Modeling of the LVSM

Fig. 4 shows the control diagram of the LVSM [9]. By emulating the electromechanical transient equation of traditional synchronous motor, the converter has similar characteristics about the inertia, active power regulation, and reactive power regulation. Moreover, in order to guarantee the input current quality of the LVSM, the input current is controlled by the quasi-proportional-resonant (PR) controller, and the current command is calculated based on the input voltage command.

The active power *P*, reactive power *Q*, and input voltage magnitude v_m of the LVSM can be calculated as follows:

$$\begin{cases} P=1.5(v_\alpha i_\alpha+v_\beta i_\beta) \\ Q=1.5(v_\beta i_\alpha-v_\alpha i_\beta) \\ v_m=\sqrt{v_\alpha^2+v_\beta^2}. \end{cases} \tag{30}$$

After imposing positive-sequence voltage perturbation at frequency f_p on the ac side of the converter, the magnitude calculation formula of the input voltage can be expressed as

$$\begin{aligned} v_m=\sqrt{v_\alpha^2+v_\beta^2}&=\{V_1^2+2V_pV_1\cos[2\pi(f_p-f_1)t+\varphi_{vp}]\}^{1/2} \\ &\approx V_1+V_p\cos[2\pi(f_p-f_1)t+\varphi_{vp}]. \end{aligned} \tag{31}$$

$$\begin{cases} A_p(s)=[H_i(s-j\omega_1)-jK_d]G_i(s) \\ B_p(s)=0 \\ C_p(s)=\{j0.5H_i(s-j\omega_1)H_m(s-j\omega_1)H_{v1}(s-j\omega_1)+[jK_d-H_i(s-j\omega_1)]\mathbf{I}_1+\mathbf{M}_1-K_f\mathbf{V}_1\}T_{\rm PLL}(s-j\omega_1)G_v(s)+K_fG_v(s) \\ F_p(s)=0.5H_{v1}(s-j\omega_1)H_i(s-j\omega_1)G_d(s-j\omega_1) \end{cases} \tag{27}$$

$$\begin{cases} A_{p2}(s)=0 \\ B_{p2}(s)=[H_i(s+j\omega_1)+jK_d]G_i(s) \\ C_{p2}(s)=\{j0.5H_i(s+j\omega_1)H_m(s+j\omega_1)H_{v1}(s+j\omega_1)+[H_i(s+j\omega_1)+jK_d]\mathbf{I}_{-1}+K_f\mathbf{V}_{-1}-\mathbf{M}_{-1}\}T_{\rm PLL}(s+j\omega_1)G_v(s+j2\omega_1) \\ F_{p2}(s)=0.5H_{v1}(s+j\omega_1)H_i(s+j\omega_1)G_d(s+j\omega_1) \end{cases} \tag{28}$$

Therefore, considering the sampling low-pass filters $G_i(s)$ and $G_v(s)$, the active power, reactive power, and voltage amplitude can be expressed in the frequency domain as follows:

$$\mathbf{P}[f]=\begin{cases}3(\mathbf{V}_{-1}\mathbf{I}_1+\mathbf{V}_1\mathbf{I}_{-1}), & f=0\\ 3[G_i(s\pm j\omega_1)\mathbf{V}_{\mp1}\mathbf{I}_{\pm p}\\ +G_v(s\pm j\omega_1)\mathbf{I}_{\mp1}\mathbf{V}_{\pm p}\\ +G_i(s\mp j\omega_1)\mathbf{V}_{\pm1}\mathbf{I}_{\pm p2}], & f=\pm(f_p-f_1)\end{cases} \tag{32}$$

$$\mathbf{Q}[f]=\begin{cases}j3(\mathbf{V}_{-1}\mathbf{I}_1-\mathbf{V}_1\mathbf{I}_{-1}), & f=0\\ \pm j3[G_i(s\pm j\omega_1)\mathbf{V}_{\mp1}\mathbf{I}_{\pm p}\\ -G_v(s\pm j\omega_1)\mathbf{I}_{\mp1}\mathbf{V}_{\pm p}\\ -G_i(s\mp j\omega_1)\mathbf{V}_{\pm1}\mathbf{I}_{\pm p2}], & f=\pm(f_p-f_1)\end{cases} \tag{33}$$

$$\mathbf{V}_m[f]=\begin{cases}V_1, & f=0\\ G_v(s\pm j\omega_1)\mathbf{V}_{\pm p}, & f=\pm(f_p-f_1)\end{cases} \tag{34}$$

where $G_v(s)=1/(1+sT_v)$ and $G_i(s)=1/(1+sT_i)$ represent the transfer functions of the voltage and current sampling filters, respectively.

According to the reactive power regulation part in Fig. 4, the magnitude e_m of the inner electric potential e_{abc} of the LVSM can be expressed in the frequency domain as follows:

$$\mathbf{e}_m[f]=\begin{cases}E_m, & f=0\\ k_q\mathbf{Q}[f]-k_v\mathbf{V}_m[f], & f=\pm(f_p-f_1)\end{cases} \tag{35}$$

where E_m represents the magnitude reference of inner electric potential; and k_q and k_v represent the reactive power control gain and ac-voltage magnitude control gain, respectively.

According to the active power regulation part in Fig. 4, the output phase perturbation $\Delta\theta$ of the controller can be obtained in the frequency domain as follows:

$$\Delta\theta_{\pm p1}=T(s)\{\mathbf{P}[\pm(f_p-f_1)]/\omega_1+G_d(s)H_{v2}(s)\mathbf{V}_{\pm dp}\} \tag{36}$$

$$T(s)=1/[Js^2+(D-P_{\rm load}/\omega_1^2)s] \tag{37}$$

where $G_d(s)=1/(1+sT_d)$ represents the transfer function of the dc-link voltage sampling filter; $H_{v2}(s)=k_{vp2}+k_{vi2}/s$ represents the transfer function of the dc-link voltage PI controller; J represents the virtual moment of inertia; D represents the droop coefficient; $P_{\rm load}$ represents the active power reference value; and k_{vp2} and k_{vi2} are proportional and integral gains of the dc-link voltage controller of the LVSM, respectively.

The sinusoidal signal generated in the LVSM control can be expressed as $\cos\theta=\cos(\theta_1+\Delta\theta)\approx\cos\theta_1-\Delta\theta\sin\theta_1$, where θ_1 represents the phase angle of the fundamental voltage. By substituting (36) and (37) into $\cos\theta$ and applying the frequency-domain convolution theorem, $\cos\theta$ can be expressed in the frequency domain as (38), shown at the bottom of this page, where $\varphi_{\rm vir}=-\arcsin[2P_{\rm load}\omega_1L_f/(3E_mV_1)]$ represents the phase difference between the inner electric potential and ac input voltage of the LVSM.

According to the electrical control part of Fig. 4, the modulating signal of the LVSM can be obtained as follows:

$$m_a=\{[G_v(s)v_a-e_m\cos\theta]/(sL_f)-G_i(s)i_a\}H_r(s) \tag{41}$$

where $H_r(s)=-[k_{rp}+k_{rr}/(s^2+2\omega_c s+\omega 2\,1)]$ is the transfer function of the quasi-PR controller in the input current loop; k_{rp}, k_{rr}, and ω_c represent proportional gain, resonance gain, and cutoff angular frequency of the quasi-PR controller, respectively.

By substituting (5)–(7), (32)–(35), and (38) into (41), and applying the frequency-domain convolution theorem, the coefficients $A(s)$, $B(s)$, $C(s)$, and $F(s)$ at frequency f_p and f_p-2f_1 in (11) can be calculated as (39), shown at the bottom of this page, and (40), shown at the bottom of this page, respectively. Similarly, by substituting (39) and (40) into the universal calculation formulas (14)–(17), the precise positive- and negative-sequence impedances $Z_{mp}(s)$ and $Z_{mn}(s)$ of the LVSM can be calculated.

III. Impedance Model Verification and Impedance Characteristics Comparison Analysis of Two Load Converters

In order to verify the impedance model of the LCVIC, the frequency responses of the derived sequence impedance models of the LCVIC and its simulation measurement results are shown in Fig. 5(a), where $Z_{cp}(s)$ and $Z_{cn}(s)$ represent the positive- and negative-sequence impedances of the LCVIC, respectively.

$$\mathbf{cos}\theta[f]=\begin{cases}0.5e^{\pm j\varphi_{\rm vir}}, & f=\pm f_1\\ \pm j0.5e^{\pm j\varphi_{\rm vir}}T(s\mp j\omega_1)\{\mathbf{P}[\pm(f_p-f_1)]/\omega_1+H_{v2}(s\mp j\omega_1)G_d(s\mp j\omega_1)\mathbf{V}_{\pm dp}\}, & f=\pm f_p\\ \mp j0.5e^{\mp j\varphi_{\rm vir}}T(s\pm j\omega_1)\{\mathbf{P}[\pm(f_p-f_1)]/\omega_1+H_{v2}(s\pm j\omega_1)G_d(s\mp j\omega_1)\mathbf{V}_{\pm dp}\}, & f=\pm(f_p-2f_1)\end{cases} \tag{38}$$

$$\begin{cases}A_p(s)=[-j3E_me^{j\varphi_{\rm vir}}T(s-j\omega_1)\mathbf{V}_{-1}/\omega_1-j3k_qe^{j\varphi_{\rm vir}}\mathbf{V}_{-1}-2sL_f]H_r(s)G_i(s)/(2sL_f)\\ B_p(s)=3e^{j\varphi_{\rm vir}}[jk_q\mathbf{V}_1-jE_mT(s-j\omega_1)\mathbf{V}_1/\omega_1]H_r(s)G_i(s-j2\omega_1)/(2sL_f)\\ C_p(s)=[-j3E_me^{j\varphi_{\rm vir}}T(s-j\omega_1)\mathbf{I}_{-1}/\omega_1+j3k_qe^{j\varphi_{\rm vir}}\mathbf{I}_{-1}+k_ve^{j\varphi_{vir}}+2]H_r(s)G_v(s)/(2sL_f)\\ F_p(s)=-jE_me^{j\varphi_{\rm vir}}T(s-j\omega_1)H_{v2}(s-j\omega_1)H_r(s)G_d(s-j\omega_1)/(2sL_f)\end{cases} \tag{39}$$

$$\begin{cases}A_{p2}(s)=3e^{-j\varphi_{\rm vir}}[jE_mT(s+j\omega_1)\mathbf{V}_{-1}/\omega_1-jk_q\mathbf{V}_{-1}]H_r(s)G_i(s+j2\omega_1)/(2sL_f)\\ B_{p2}(s)=[-2sL_f+j3E_me^{-j\varphi_{\rm vir}}T(s+j\omega_1)\mathbf{V}_1/\omega_1+j3k_qe^{-j\varphi_{\rm vir}}\mathbf{V}_1]H_r(s)G_i(s)/(2sL_f)\\ C_{p2}(s)=3e^{-j\varphi_{\rm vir}}[jE_mT(s+j\omega_1)\mathbf{I}_{-1}+jk_q\mathbf{I}_{-1}+k_v]H_r(s)G_v(s+j2\omega_1)/(2sL_f)\\ F_{p2}(s)=jE_me^{-j\varphi_{\rm vir}}T(s+j\omega_1)H_{v2}(s+j\omega_1)H_r(s)G_d(s+j\omega_1)/(2sL_f)\end{cases} \tag{40}$$

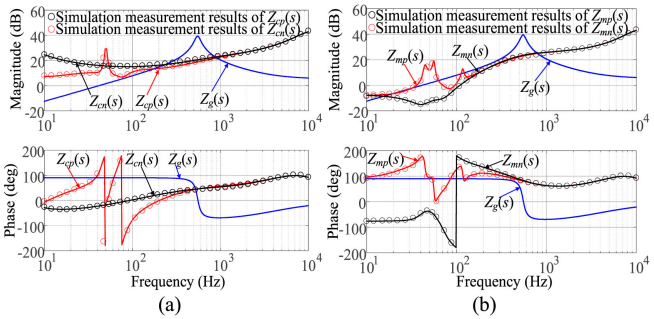

Fig. 5. Frequency responses of the derived sequence impedance models of two load converters and their simulation measurement results. (a) LCVIC. (b) LVSM.

TABLE I
SYSTEM PARAMETERS OF THE LCVIC

Symbol	Value	Symbol	Value
V_{dc}	700 V	T_i	44 μs
V_g	220 V	T_d	1 ms
L_f	2 mH	k_{pp}	0.833
C_f	22 μF	k_{pi}	107.86
R_f	1.87 Ω	k_{ip}	0.00857
C_{dc}	3 mF	k_{ii}	1.143
L_g	3.8 mH	k_{vp1}	1
P_{load}	10 kW	k_{vi1}	43
I_{qr}	0 A	$K_{\omega v}$	23 V/(rad/s)
f_1	50 Hz	K	k_{pp}
f_s	10 kHz	K_d	0.0018
T_v	44 μs	K_f	0.0029

TABLE II
SYSTEM PARAMETERS OF THE LVSM

Symbol	Value	Symbol	Value
V_{dc}	700 V	T_v	44 μs
V_g	220 V	T_i	44 μs
L_f	2 mH	T_d	1 ms
C_f	22 μF	J	0.0202 kg·m^2
R_f	1.87 Ω	D	3.8 N·m·s/rad
C_{dc}	3 mF	k_q	5×10^{-3}
L_g	3.8 mH	k_v	10×10^{-1}
P_{load}	10 kW	k_{vp2}	0.3183
Q_r	0 kVar	k_{vi2}	5
V_1	311 V	k_{rp}	0.00286
E_0	305 V	k_{rr}	0.7143
f_1	50 Hz	ω_c	10 rad/s
f_s	10 kHz		

$Z_g(s)$ represents the grid impedance. The system parameters of the LCVIC are shown in Table I, which are calculated according to the parameter design method in [11]. From Fig. 5(a), the simulation measurement results coincide with the derived sequence impedance models, which verify the accuracy of the derived sequence impedance model of the LCVIC.

Similarly, in order to verify the impedance model of the LVSM, the frequency responses of the derived sequence impedance models of the LVSM and its simulation measurement results are shown in Fig. 5(b), where $Z_{mp}(s)$ and $Z_{mn}(s)$ represent the positive- and negative-sequence impedances of the LVSM, respectively. The control parameters of the LVSM are shown in Table II, which are calculated according to the parameter design method in [9]. From Fig. 5(b), the simulation measurement results also coincide with the derived sequence impedance models, which verify the accuracy of the derived sequence impedance model of the LVSM.

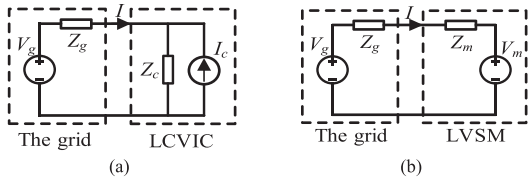

Fig. 6. Small-signal equivalent circuit. (a) LCVIC. (b) LVSM.

Moreover, according to Fig. 5, the sequence impedance characteristics of the two load converters are compared as follows.

1) The positive-sequence impedance of the LCVIC exhibits the negative-resistive-capacitive characteristic (i.e., the phase angle is between $-180°$ and $-90°$) in the middle-frequency band, and its amplitude–frequency curve easily intersects with $Z_g(s)$ in this frequency band when the grid becomes weakened. Furthermore, $Z_g(s)$ presents inductive characteristic in the low- and middle-frequency bands. Therefore, the impedance characteristics of the LCVIC make it easy to interact with $Z_g(s)$, which can result in harmonic oscillation.
2) The positive-sequence impedance of the LVSM exhibits the inductive characteristic in the middle-frequency band, which is basically consistent with the impedance characteristic of $Z_g(s)$. Moreover, the negative-sequence impedance of the LVSM exhibits the negative-resistive-capacitive characteristic only in the middle-frequency band, and its amplitude is much smaller than $Z_g(s)$ in this frequency band. Therefore, the LVSM has better impedance characteristics to avoid harmonic oscillation in the weak grid.

IV. STABILITY COMPARISON ANALYSIS OF TWO LOAD CONVERTERS

A. Impedance Ratio Criterion Analysis

In this article, the precise SISO sequence impedance model is derived, and thus, the NSC can be applied to analyze the interaction stability between the load converter and the grid. In Fig. 6(a), the LCVIC is considered as a current-controlled converter and can be equivalent to a current source (I_c) in parallel with an input impedance (Z_c) [30]. Therefore, the input current can be calculated as follows:

$$I(s)=\left[\frac{V_g(s)}{Z_c(s)}-I_c(s)\right]\frac{1}{1+Z_g(s)/Z_c(s)}. \tag{42}$$

Because the ideal grid voltage $V_g(s)$ is stable when unloaded and the LCVIC can maintain stable when powered from the ideal grid, i.e., $1/Z_c(s)$ has no poles in the right-half plane (RHP), so that the system stability depends on $1/[1+Z_g(s)/Z_c(s)]$. Since the impedance ratio $Z_g(s)/Z_c(s)$ has no RHP poles, it is feasible to check simply whether the Nyquist plots of $Z_g(s)/Z_c(s)$ encircle $(-1, j\,0)$ to judge the stability.

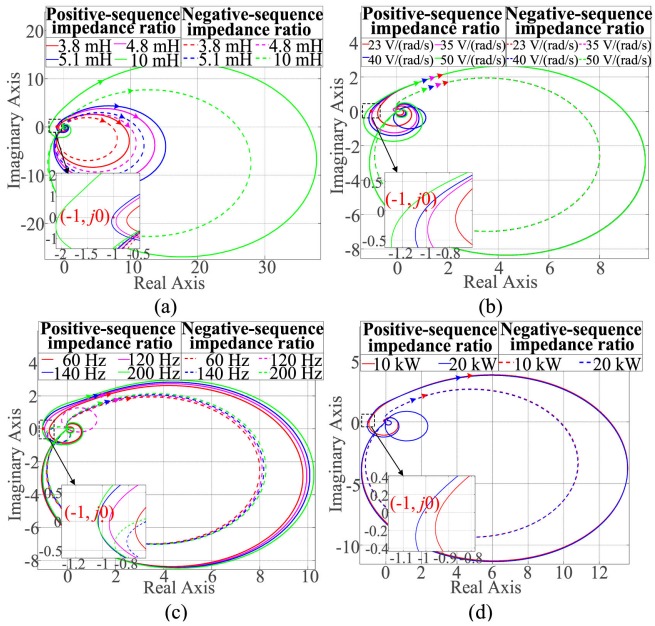

Fig. 7. Nyquist plots of LCVIC impedance ratios for stability assessment with different parameters. (a) Different L_g when $K_{\omega v} = 23$ V/(rad/s), $\mathrm{BW_{PLL}} = 60$ Hz, and $P_{\mathrm{load}} = 10$ kW. (b) Different $K_{\omega v}$ when $L_g = 3.8$ mH, $\mathrm{BW_{PLL}} = 60$ Hz, and $P_{\mathrm{load}} = 10$ kW. (c) Different $\mathrm{BW_{PLL}}$ when $L_g = 3.8$ mH, $K_{\omega v} = 23$ V/(rad/s), and $P_{\mathrm{load}} = 10$ kW. (d) Different P_{load} when $L_g = 4.8$ mH, $K_{\omega v} = 23$ V/(rad/s), and $\mathrm{BW_{PLL}} = 60$ Hz.

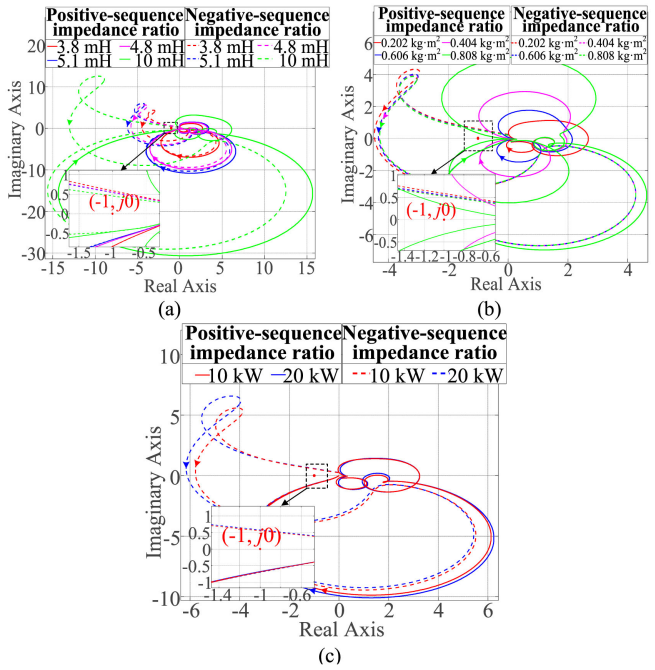

Fig. 8. Nyquist plots of the LVSM impedance ratios for stability assessment with different parameters. (a) Different L_g when $J = 0.202$ kg·m^2 and $P_{\mathrm{load}} = 10$ kW. (b) Different J when $L_g = 3.8$ mH and $P_{\mathrm{load}} = 10$ kW. (c) Different P_{load} when $L_g = 4.8$ mH and $J = 0.202$ kg·m^2.

In Fig. 6(b), the LVSM is considered as a voltage-controlled converter and can be equivalent to a voltage source (V_m) in series with an input impedance (Z_m) [30]. Hence, the input current can be calculated as follows:

$$I(s) = (V_g(s) - V_m(s))\frac{1}{Z_m(s) + Z_g(s)} = (V_g(s) - V_m(s))\frac{1/Z_m(s)}{1 + Z_g(s)/Z_m(s)}. \quad (43)$$

Because the ideal grid voltage $V_g(s)$ and the ideal equivalent output voltage of LVSM $V_m(s)$ are stable, so that the system stability depends on $1/[Z_m(s) + Z_g(s)]$. Generally, the order of denominator is required to be higher than the numerator of the open-loop transfer function when applying the NSC. Thus, the Nyquist plot can converge to the origin with the increase of frequency, and it is convenient to judge the stability. Since the order of $Z_m(s)$ is generally higher than that of $Z_g(s)$, the impedance ratio $Z_g(s)/Z_m(s)$ is used to judge the stability. The grid impedance $Z_g(s)$ has no RHP poles, so the system is stable when the number of counterclockwise encirclements of the point $(-1, j\,0)$ by the Nyquist plot of $Z_g(s)/Z_m(s)$ equals the number of RHP zeros of $Z_m(s)$.

B. Stability Comparison Analysis of the LCVIC and the LVSM

Fig. 7 shows the Nyquist plots (frequency from 0 to 10^5 Hz) of the impedance ratios of the LCVIC with different parameters. From Fig. 7(a), the system tends to be unstable with the increase of L_g. When $L_g \geq 5.1$ mH, the Nyquist plot encircles $(-1, j\,0)$ and the system is unstable. In Fig. 7(b), when the inertia control gain $K_{\omega v} \geq 40$ V/(rad/s), the Nyquist plot of the positive-sequence impedance ratio encircles $(-1, j\,0)$ and the system is unstable. From Fig. 7(c), the system becomes unstable with the increase of PLL bandwidth ($\mathrm{BW_{PLL}}$). When $\mathrm{BW_{PLL}} \geq 140$ Hz, the Nyquist plot encircles $(-1, j\,0)$ and the system is unstable. In Fig. 7(d), when the load power is increased to 20 kW, the Nyquist plot of the positive-sequence impedance ratio encircles $(-1, j\,0)$, which implies that the increase of the LCVIC load power can cause the instability under weak grids.

Fig. 8 shows the Nyquist plots (frequency from 0 to 10^5 Hz) of impedance ratios of the LVSM with different parameters. The frequency response curves in Fig. 5(b) reveal that the sequence impedances of the LVSM has no RHP zeros, whereas the negative-sequence impedance of the LVSM has a pair of RHP conjugate zeros due to the existence of the second-order differential element [31]. Therefore, when the Nyquist plot of the positive-sequence impedance ratio does not encircle $(-1, j\,0)$, and the positive-frequency Nyquist plot of the negative-sequence impedance ratio crosses the real axis at the left of $(-1, j\,0)$ once in the counterclockwise direction, the system is stable. From Fig. 8(a), the LVSM can remain stable when L_g is increased to 10 mH. From Fig. 8(b), the system is stable even if J is increased fourfold. From Fig. 8(c), when the load power of the LVSM is increased to 20 kW, the LVSM is still stable. Therefore, the LVSM has better stability than the LCVIC in the weak grid.

V. Experimental Results

In order to verify the stability analysis results presented in the previous sections, the experimental prototype of the three-phase

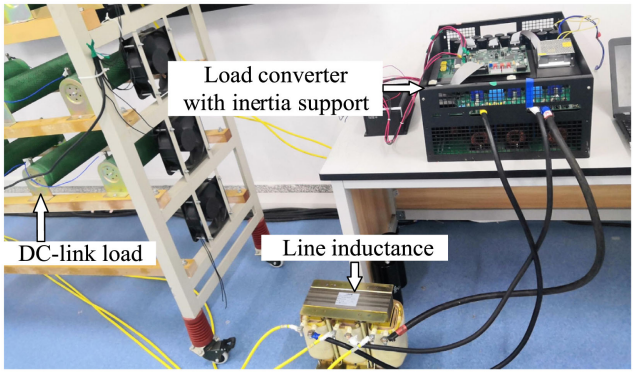

Fig. 9. Experimental prototype of the three-phase load converter connected to the weak grid.

load converter is built in the weak grid, as shown in Fig. 9. The LCVIC and the LVSM have the same topology, and the parameters are shown in Tables I and II, respectively. Their control system is implemented in the DSP+FPGA. Specifically, the DSP TMS320F2812 is used to realize the control algorithm, and the FPGA EP2C8Q208CN is used to acquire current and voltage sampling signals and transmit data to the DSP and the liquid crystal. Meanwhile, the high-speed A/D chip ADS8556 is used to sample current and voltage. The switching frequency f_s is selected as 10 kHz. The weak grid is emulated by the utility grid in series with line inductance.

Under different parameters, the experimental waveforms and the harmonic spectra analyses of the LCVIC and the LVSM are shown in Figs. 10 and 11, respectively. From Fig. 10(a), when L_g is increased from 4.8 to 5.1 mH, the input currents of the LCVIC start to divergently oscillate at 97 and 3 Hz (the coupling frequency). In Fig 10(b), when $K_{\omega v}$ is increased from 35 to 40 V/(rad/s), the input currents of the LCVIC start to divergently oscillate at 99 and 1 Hz (the coupling frequency). From Fig. 10(c), when $\mathrm{BW_{PLL}}$ is increased from 120 to 140Hz, the input currents of the LCVIC start to divergently oscillate at 123 and 23 Hz (the coupling frequency). In Fig. 10(d), when the load power is increased from 10 to 20 kW, the input currents of the LCVIC start to divergently oscillate at 96 and 4 Hz (the coupling frequency). Furthermore, Fig 10 shows that the divergent currents are triggering the overcurrent protection over time. However, from Fig. 11, the input current of the LVSM remains stable no matter L_g is increased to 10 mH, J is increased to 0.808 kg·m^2, or the load power is increased to 20 kW. Therefore, the experimental results are consistent with the stability analysis results based on the NSC in Section IV, which reveals that the LVSM has better stability than the LCVIC in the weak grid.

Moreover, Fig. 12 shows the frequency responses predicted by the derived models of the LCVIC under different experimental parameters. When the phase difference between the LCVIC impedance and the grid impedance is greater than 180° at their magnitude intersection frequency, the system is unstable and oscillates at the corresponding frequency. Therefore, from Fig. 12, the oscillation frequencies predicted by the derived models match the harmonic spectra analyses of the experimental waveforms in Fig. 10, which further validate the correctness of the derived SISO sequence impedance models.

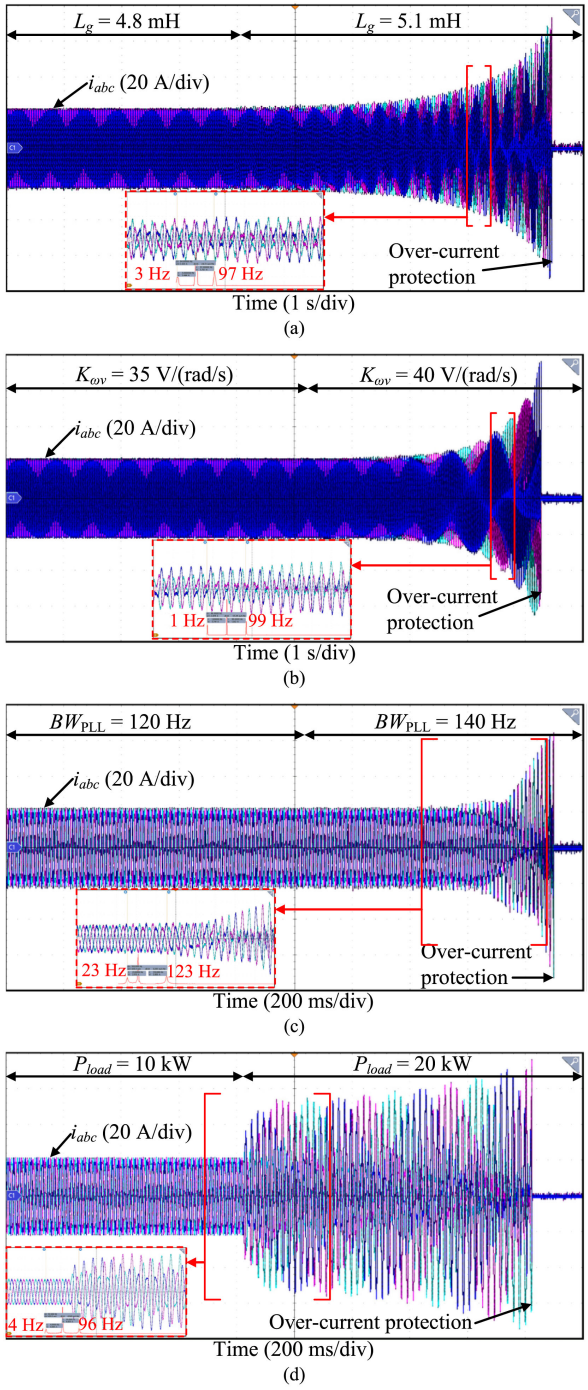

Fig. 10. Experimental waveforms and harmonic spectra analyses of the LCVIC with different parameters. (a) L_g is increased from 4.8 to 5.1 mH when $K_{\omega v}$ = 23 V/(rad/s), $\mathrm{BW_{PLL}}$ = 60 Hz, and P_{load} = 10 kW. (b) $K_{\omega v}$ is increased from 35 to 40 V/(rad/s) when L_g = 3.8 mH, $\mathrm{BW_{PLL}}$ = 60 Hz, and P_{load} = 10 kW. (c) $\mathrm{BW_{PLL}}$ is increased from 120 to 140 Hz when L_g = 3.8 mH, $K_{\omega v}$ = 23 V/(rad/s), and P_{load} = 10 kW. (d) P_{load} is increased from 10 to 20 kW when L_g = 4.8 mH, $K_{\omega v}$ = 23 V/(rad/s), and $\mathrm{BW_{PLL}}$ = 60 Hz.

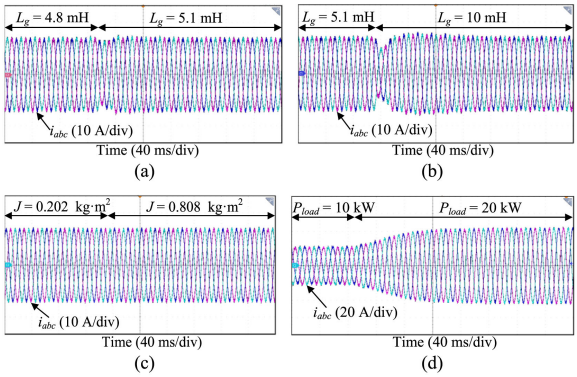

Fig. 11. Experimental waveforms of the LVSM with different grid inductance values. (a) L_g is increased from 4.8 to 5.1 mH when $J = 0.202$ kg·m^2 and $P_{\rm load} = 10$ kW. (b) L_g is increased from 5.1 to 10 mH when $J = 0.202$ kg·m^2 and $P_{\rm load} = 10$ kW. (c) J is increased from 0.202 to 0.808 kg·m^2 when $L_g = 3.8$ mH and $P_{\rm load} = 10$ kW. (d) $P_{\rm load}$ is increased from 10 to 20 kW when $L_g = 4.8$ mH and $J = 0.202$ kg·m^2.

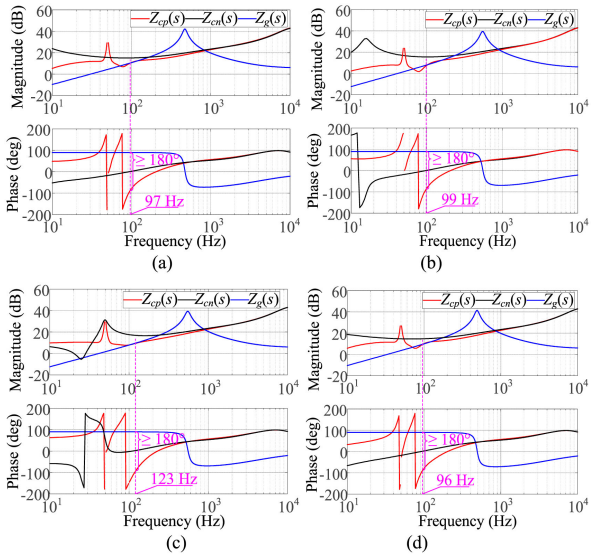

Fig. 12. Frequency responses for the sequence impedances of the LCVIC corresponding to different experimental parameters. (a) When $L_g = 5.1$ mH in Fig. 10(a). (b) When $K_{\omega v} = 40$ V/(rad/s) in Fig. 10(b). (c) When $\rm BW_{PLL} = 140$ Hz in Fig. 10(c). (d) When $P_{\rm load} = 20$ kW in Fig. 10(d).

VI. Conclusion

In this article, considering the dc-link voltage dynamics and frequency-coupling effects, the precise SISO sequence impedance models were established for the LCVIC and the LVSM. Based on the derived impedance model and NSC, the stabilities of two load converters in the weak grid have been analyzed and compared from the perspective of sequence impedance. The following conclusions are drawn.

1) The positive-sequence impedance of the LVSM exhibits inductive characteristic in the middle-frequency band, which is basically consistent with the grid impedance characteristic. Nevertheless, the positive-sequence impedance of the LCVIC exhibits negative-resistive-capacitive characteristic in the middle-frequency band, and its amplitude-frequency curve easily intersects with the grid impedance in this frequency band when the grid becomes weakened.
2) The interaction stability between the LCVIC and the grid is affected by the inertia control gain, the PLL bandwidth, the grid inductance, and the load power. The larger they are, the easier the converter is to oscillate.
3) The impedance characteristics of LVSM are conducive to avoiding harmonic oscillation in the weak grid. In contrast, the impedance characteristics of the LCVIC make it easy to interact with the grid impedance, resulting in harmonic oscillation. Therefore, the LVSM has better stability than the LCVIC in the weak grid.

References

[1] N. Pogaku, M. Prodanovic, and T. C. Green, "Modeling, analysis and testing of autonomous operation of an inverter-based microgrid," *IEEE Trans. Power Electron.*, vol. 22, no. 2, pp. 613–625, Mar. 2007.
[2] N. Flourentzou, V. G. Agelidis, and G. D. Demetriades, "VSC-based HVDC power transmission systems: An overview," *IEEE Trans. Power Electron.*, vol. 24, no. 3, pp. 592–602, Mar. 2009.
[3] B. Singh, B. N. Singh, A. Chandra, K. Al-Haddad, A. Pandey, and D. P. Kothari, "A review of three-phase improved power quality AC-DC converters," *IEEE Trans. Ind. Electron.*, vol. 51, no. 3, pp. 641–660, Jun. 2004.
[4] M. Yilmaz and P. T. Krein, "Review of battery charger topologies, charging power levels, and infrastructure for plug-in electric and hybrid vehicles," *IEEE Trans. Power Electron.*, vol. 28, no. 5, pp. 2151–2169, May 2013.
[5] Q. Zhong and G. Weiss, "Synchronverters: Inverters that mimic synchronous generators," *IEEE Trans. Ind. Electron.*, vol. 58, no. 4, pp. 1259–1267, Apr. 2011.
[6] Q. Zhong, Z. Ma, and P. Nguyen, "PWM-controlled rectifiers without the need of an extra synchronisation unit," in *Proc. 38th Annu. Conf. IEEE Ind. Electron. Soc.*, Montreal, QC, Canada, 2012, pp. 691–695.
[7] J. Jia, Y. Yang, and K. Ji, "Unbalanced voltage improvement control of virtual synchronous rectifier," in *Proc. 8th Annu. Int. Conf. CYBER Technol. Autom., Control, Intell. Syst.*, Tianjin, China, 2018, pp. 1171–1176.
[8] R. Aouini, B. Marinescu, K. Kilani, and M. Elleuch, "Synchronverter based emulation and control of HVDC transmission," *IEEE Trans. Power Syst.*, vol. 31, no. 1, pp. 278–286, Jan. 2016.
[9] B. Gao, C. Xia, L. Zhang, and N. Chen, "Modeling and parameters design for rectifier side of VSC-HVDC based on virtual synchronous machine technology," *Proc. CSEE*, vol. 37, no. 2, pp. 534–543, Jan. 2017.
[10] J. Fang, H. Li, Y. Tang, and F. Blaabjerg, "Distributed power system virtual inertia implemented by grid-connected power converters," *IEEE Trans. Power Electron.*, vol. 33, no. 10, pp. 8488–8499, Oct. 2018.
[11] J. Fang, P. Lin, H. Li, Y. Yang, and Y. Tang, "An improved virtual inertia control for three-phase voltage source converters connected to a weak grid," *IEEE Trans. Power Electron.*, vol. 34, no. 9, pp. 8660–8670, Sep. 2019.
[12] B. Wen, D. Boroyevich, R. Burgos, P. Mattavelli, and Z. Shen, "Small-signal stability analysis of three-phase AC systems in the presence of constant power loads based on measured d-q frame impedances," *IEEE Trans. Power Electron.*, vol. 30, no. 10, pp. 5952–5963, Oct. 2015.
[13] B. Wen, D. Dong, D. Boroyevich, R. Burgos, P. Mattavelli, and S. Zhiyu, "Impedance-based analysis of grid-synchronization stability for three-phase paralleled converters," *IEEE Trans. Power Electron.*, vol. 31, no. 1, pp. 26–38, Jan. 2016.
[14] D. Lu, X. Wang, and F. Blaabjerg, "Impedance-based analysis of dc-link voltage dynamics in voltage-source converters," *IEEE Trans. Power Electron.*, vol. 34, no. 4, pp. 3973–3985, Apr. 2019.
[15] C. Li, R. Burgos, B. Wen, Y. Tang, and D. Boroyevich, "Analysis of STATCOM small-signal impedance in the synchronous D-Q frame," *IEEE J. Emerg. Sel. Topics Power Electron.*, vol. 35, no. 3, pp. 2268–2283, Mar. 2020.
[16] J. Sun, "Small-signal methods for AC distributed power systems: A review," *IEEE Trans. Power Electron.*, vol. 24, no. 11, pp. 2545–2554, Nov. 2009.

[17] M. Cespedes and J. Sun, "Impedance modeling and analysis of grid-connected voltage-source converters," *IEEE Trans. Power Electron.*, vol. 29, no. 3, pp. 1254–1261, Mar. 2014.
[18] H. Liu and J. Sun, "Voltage stability and control of offshore wind farms with AC collection and HVDC transmission," *IEEE J. Emerg. Sel. Topics Power Electron.*, vol. 2, no. 4, pp. 1181–1189, Dec. 2014.
[19] I. Vieto and J. Sun, "Sequence impedance modeling and analysis of Type-III wind turbines," *IEEE Trans. Energy Convers.*, vol. 33, no. 2, pp. 537–545, Jun. 2018.
[20] J. Sun and H. Liu, "Sequence impedance modeling of modular multilevel converters," *IEEE J. Emerg. Sel. Topics Power Electron.*, vol. 5, no. 4, pp. 1427–1443, Dec. 2017.
[21] W. Wu *et al.*, "Sequence impedance modeling and stability comparative analysis of voltage-controlled VSGs and current-controlled VSGs," *IEEE Trans. Ind. Electron.*, vol. 66, no. 8, pp. 6460–6472, Aug. 2019.
[22] W. Wu *et al.*, "Sequence-impedance-based stability comparison between VSGs and traditional grid-connected inverters," *IEEE Trans. Power Electron.*, vol. 34, no. 1, pp. 46–52, Jan. 2019.
[23] X. Wang and F. Blaabjerg, "Harmonic stability in power electronic-based power systems: concept, modeling, and analysis," *IEEE Trans. Smart Grid*, vol. 10, no. 3, pp. 2858–2870, May 2019.
[24] C. Zhang, X. Cai, A. Rygg, and M. Molinas, "Sequence domain SISO equivalent models of a grid-tied voltage source converter system for small-signal stability analysis," *IEEE Trans. Energy Convers.*, vol. 33, no. 2, pp. 741–749, Jun. 2018.
[25] A. Rygg, M. Molinas, C. Zhang, and X. Cai, "A modified sequence-domain impedance definition and its equivalence to the dq-domain impedance definition for the stability analysis of AC power electronic systems," *IEEE J. Emerg. Sel. Topics Power Electron.*, vol. 4, no. 4, pp. 1383–1396, Dec. 2016.
[26] A. Rygg, M. Molinas, C. Zhang, and X. Cai, "On the equivalence and impact on stability of impedance modelling of power electronic converters in different domains," *IEEE J. Emerg. Sel. Topics Power Electron.*, vol. 5, no. 4, pp. 1444–1454, Dec. 2017.
[27] V. Blasko and V. Kaura, "A new mathematical model and control of a three-phase AC–DC voltage source converter," *IEEE Trans. Power Electron.*, vol. 12, no. 1, pp. 116–123, Jan. 1997.
[28] M. K. Bakhshizadeh *et al.*, "Couplings in phase domain impedance modeling of grid-connected converters," *IEEE Trans. Power Electron.*, vol. 31, no. 10, pp. 6792–6796, Oct. 2016.
[29] X. Wang, L. Harnefors, and F. Blaabjerg, "A unified impedance model of grid-connected voltage-source converters," *IEEE Trans. Power Electron.*, vol. 33, no. 2, pp. 1775–1787, Feb. 2018.
[30] J. Sun, "Impedance-based stability criterion for grid-connected inverters," *IEEE Trans. Power Electron.*, vol. 26, no. 11, pp. 3075–3078, Mar. 2011.
[31] Y. Liao and X. Wang, "Impedance-based stability analysis for interconnected converter systems with open-loop RHP poles," *IEEE Trans. Power Electron.*, vol. 35, no. 4, pp. 4388–4397, Apr. 2020.

Yifeng Liu was born in Hunan, China, 1994. He received the B.S. degree in electrical engineering from the the Hunan Institute of Engineering, Xiangtan, China, in 2016. He is currently working toward the Ph.D. degree in electrical engineering with Hunan University, Changsha, China.

His research interests include modeling and control of power electronic converters, distributed generation, and HVdc systems.

Xiaoping Zhou (Student Member, IEEE) was born in Jiangxi, China, 1990. He received the B.S. and Ph.D. degrees in electrical engineering from Hunan University, Changsha, China, in 2013 and 2018, respectively.

He is currently a Postdoctoral Research of Electrical Engineering with Hunan University. His research interests include power electronics, distributed generation, microgrid, power quality, and energy storage.

Yandong Chen (Senior Member, IEEE) was born in Hunan, China, in 1979. He received the B.S. and M.S. degrees in instrument science and technology and the Ph.D. degree in electrical engineering from Hunan University, Changsha, China, in 2003, 2006, and 2014, respectively.

He is currently a Professor with the College of Electrical and Information Engineering, Hunan University. His research interests include power electronics for microgrid, distributed generation, power quality, and energy storage.

Dr. Chen is a recipient of the 2014 National Technological Invention Awards of China, and the 2014 WIPO-SIPO Award for Chinese Outstanding Patented Invention. He is a Member of IEEE Power Electronics Society.

Leming Zhou (Member, IEEE) was born in Hunan, China, in 1989. He received the B.S. and Ph.D. degrees in electrical engineering from Hunan University, Changsha, China, in 2011 and 2016, respectively.

He is currently an Associate Professor of electrical engineering with Hunan University. His research interests include power electronics, electric power green transformation, distributed generation, and marine special power supply.

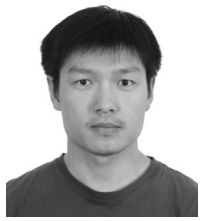

Lei Wang (Member, IEEE) received the B.Sc. degree in electrical and electronics engineering from the University of Macau (UM), Macao, in 2011, the M.Sc. degree in electronics engineering from the Hong Kong University of Science and Technology, Hong Kong, in 2012, and the Ph.D. degree in electrical and computer engineering from UM in 2017.

He was a Postdoctoral Fellow with the Power Electronics Laboratory, UM, from January 2017 to February 2019. He was a Visiting Fellow with the Department of Electrical and Computer Engineering, University of Auckland, from February 2019 to August 2019. In 2019, he joined the College of Electrical and Information Engineering, Hunan University, Changsha, China, where he is currently a Full Professor. He has authored one Springer books, one Elsevier book chapter, five patents (USA and China), and more than 30 journal and conference papers.

Dr. Wang was the recipient of the Champion Award in the "Schneider Electric Energy Efficiency Cup," Hong Kong, in 2011, and the Macao Science and Technology R&D Award for Postgraduates (Ph.D.) in 2018.

Wenhua Wu (Student Member, IEEE) was born in Hunan, China, 1991. He received the B.S. and Ph.D. degrees from the College of Electrical and Information Engineering, Hunan University, Changsha, China, in 2014 and 2019, respectively.

He is currently a Postdoctoral Research of electrical engineering with Hunan University. His research interests include renewable energy generation systems, microgrid, power quality, and VSC-HVdc systems.